IGC Newsletter

From the Editor's Desk

Dear Reader

It is my pleasant privilege to forward the latest issue of IGC Newsletter (Volume 130, October 2021, Issue 4). I thank my team for their timely inputs, cooperation and support in bringing out this issue.

The digital copy is published through the websites http://vaigai and http://www.igcar.gov.in. Additionally, on the Vaigai website, the flip copy of the Newsletter is available.

The first technical article is on "Studies on the Development of HydroxyAcetamide based Novel Extractant for the Treatment of High-Level Waste Solutions". The article is contributed by Dr. T. Prathibha and his colleagues from the Materials Chemistry & Metal Fuel Cycle Group.

The second technical article is on "Stability of B1-type Oxides in BCC Iron by Density Functional Theory Calculations". The article is contributed by Dr. Chinnappan Ravi and his colleagues from the Materials Science Group.

Young Researcher's Forum features an article on "Fabrication of Graphene Oxide-nano SiO_2-Polydimethylsiloxane Composite Coating on Carbon Steel" by Ms. Geetisubhra Jena from Metallurgy & Materials Group, IGCAR.

We are happy to share with you the awards, honours and distinctions earned by our colleagues and about the important events.

The back cover of the IGC Newsletter has Indian Silverbill this time .

The Editorial Committee would like to thank all the contributors. We look forward to receiving constructive suggestions from readers towards improving the IGC Newsletter content.

Use Face Mask. Maintain Social Distance to break the chain. Vaccinate. Stay Safe.

With best wishes and regards

S. Rajeswari
Chairman, Editorial Committee, IGC Newsletter and
Head, Scientific Information Resource Division, IGCAR

Studies on the Development of HydroxyAcetamide based Novel Extractant for the Treatment of High-Level Waste Solutions

The nuclear power program of our country envisages the operation of a closed nuclear fuel cycle, where reprocessing of spent fuel plays an integral role. The radiotoxicity of the spent fuel is considerably reduced by the removal and re-use of plutonium isotopes along with uranium during the reprocessing steps. Aqueous reprocessing based on the PUREX process has been successfully carried out in the reprocessing plants of India and many other countries for the past few decades. The aqueous raffinate after the PUREX process contains all the fission products and heavier actinides generated during the reactor operation and is generally known as the 'high-level liquid waste' (HLLW), due to the enormous radiotoxicity contained it. Direct vitrification of HLLW in a suitable glass or ceramic matrix and disposal into deep geological repositories would demand the surveillance of such geological repositories for millions of years. A smaller fraction of heavier actinides, commonly described as the 'minor actinides' including the alpha emitting radionuclides of neptunium, americium and curium have been identified as the major contributors for the radio toxicity of HLLW. Selective partitioning of these long-lived radio nuclides significantly reduces the radiotoxicity of HLLW and hence this partitioning step is considered as an essential part of closed nuclear fuel cycles. In the Indian context, the partitioned minor actinides could be burned in the fast breeder reactor systems scheduled for commissioning in the future. It is also proposed to transmute them into shorter-lived nuclides in accelerator driven systems (ADS) being developed for this purpose in different parts of the world.

Partitioning of minor actinides from HLLW is 'need of the hour' for many countries in the European Union, Japan, Russia, and the United States, where considerable amounts of HLLW has been generated by several years of reprocessing activities. Separation processes based on solvent extraction methods have been widely studied in this area. This involves a challenging task of separating only a small fraction of highly alpha active actinides from the bulk of chemically similar lanthanides and other fission products in HLLW. Ligands based on diglycolamides such as N,N,N',N'-tetraoctyldiglycolamide (TODGA) and N,N,N',N'-tetra(2-ethylhexyl)diglycolamide (TEHDGA) are the best promising organic extractants identified for minor actinide partitioning (Figure 1). In India, an Actinide Separation Demonstration Facility (ASDF) was commissioned at BARC, Tarapur in 2013 for the demonstration of removal of alpha activity from HLLW, based on many years of R&D expertise in this area. There is a continued interest in developing advanced reagents for a cleaner separation of minor actinides for their efficient re-use in ADS or fast reactors.

Extractants for minor actinide partitioning-role of aggregation behavior

Due to safety concerns, only non-polar diluents such as n-dodecane or NPH (normal paraffinic hydrocarbon) are recommended for solvent extraction processes in nuclear industry. In comparison to the ligands employed for reprocessing applications (e.g. Tri-n-butyl phosphate, TBP), the ligands with more numbers of polar groups are useful for the treatment of HLLW. These polar ligands are made soluble in non-polar diluents by attaching long alkyl chains (Figure 1). When such molecules are dissolved in non-polar diluents, they undergo self-aggregation into groups known
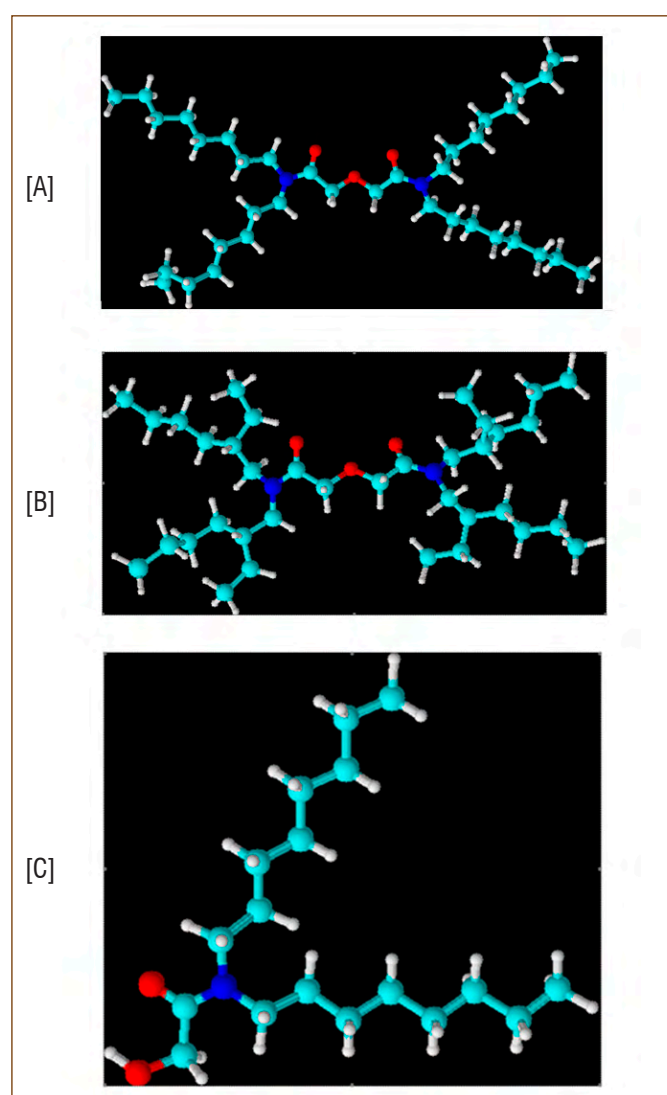

Figure 1: 3D structures of N,N,N',N'-tetraoctyldiglycolamide (TODGA) [A], N,N,N',N'-tetra(ethylhexyl)diglycolamide (TEHDGA) [B] and N,N-di-octyl-2-hydroxyacetamide [C]. The co-ordinating oxygen atoms are shown in red, nitrogens in blue, carbons in cyan and hydrogens in white.
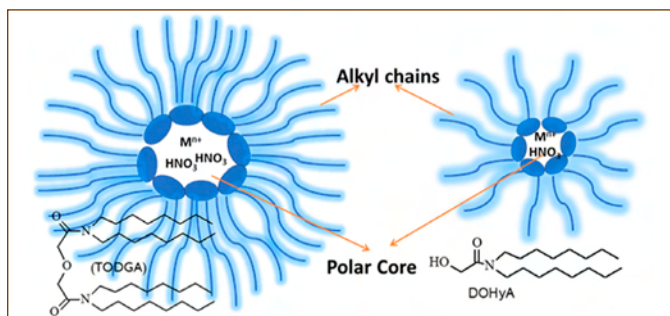
Figure 2: Schematic of the reverse micelles formed by different extractants

as the 'reverse micelles' with their polar groups turning to the center and non-polar tails at the periphery (Figure 2).

During the solvent extraction process, polar moieties such as water, nitric acid and metal ions are extracted from the aqueous phase into the organic phase. They are usually trapped in the polar cores of the reverse micellar aggregates, resulting in swelling of these aggregates. The dispersive forces between the non-polar tails of reverse micellar aggregates helps to stabilize them in the non-polar medium of organic phase, whereas the attractive interactions between the polar cores tend to de-stabilize and merge the aggregates. As the loading of organic phase increases, the merger of aggregates eventually results in the splitting of organic phase into a light phase rich with diluent, and a heavy phase known as the 'third phase' which is holding major fraction of extractants and extracted species.

The third phase formation is a serious concern during solvent extraction processes in nuclear industry, as the un-intended accumulation of fissile materials in third phase could lead to criticality accidents. The diglycolamides, TODGA and TEHDGA are highly prone to third phase formation and this is usually avoided by using a suitable co-extractant, commonly described as a 'phase modifier'. A less polar ligand such as a long chain monoamide or a long chain alcohol is added as a phase modifier along with the diglycolamides during the process conditions and the applicability of such combined solvents for minor actinide partitioning has been demonstrated even in hot runs with genuine HLLW solutions. Studies have shown that phase modifiers help to stabilize the reverse micellar aggregates by improving the dispersive interactions among the aggregates, thereby preventing the merger of aggregates into third phase. Despite these essential advantages, addition of phase modifiers poses some disadvantages such as increase in viscosity of solvent phase, extraction of undesirable metal ions and difficulties during back extraction of metal ions. Alcohol based phase modifiers are more prone to radiolytic degradation and flammability hazards. Therefore, it is desirable to avoid the use of a phase modifier by developing ligands which do not form third phase during the extraction of metal ions from HLLW.

As the long alkyl chains attached to the diglycolamide molecules enabled the stabilization of reverse micelles in non-polar diluents, increasing the length of alkyl chains in diglycolamides offered 'modifier-free' ligands. However, the synthesis of such ligands was not easy as TODGA or TEHDGA. In this context, a novel ligand based on hydroxyacetamides namely, N,N-di-octylhydroxyacetamide (DOHyA) (see Figure 1) was studied by our group for the treatment of HLLW. This molecule contained half the molecule of TODGA and had been identified among the radiolytic degradation products of TODGA. The synthesis of DOHyA was easier than TODGA or TEHDGA and it was found that this ligand was inherently stable towards third phase formation.

Extraction and aggregation behavior of DOHyA

HLLW contains several fission products and minor actinides dissolved in 3-4 M nitric acid solution. Usually neutral extractants are employed for the extraction of metal ions from moderately acidic solutions and these extracted metal ions are back extracted into an aqueous phase at lower acidity for recovery of the extracted metal ions from the solvent phase. Both the extraction and back extraction steps are significant in solvent extraction processes. Figure 3 compares the distribution of Am(III) in TODGA and DOHyA solvents at different acidities of aqueous phase. The distribution ratio of Am(III) ($D_{Am(III)}$) increased with increase in nitric acid concentration in both the cases. The $D_{Am(III)}$ values were higher for TODGA at lower aqueous phase acidities; however the results were similar for both the extractants at higher acidities. The DAm(III) values for DOHyA were sufficiently lower at 0.5 M and 1 M nitric acid, indicating the feasibility of back extraction of Am(III) under those conditions. This was an important advantage of DOHyA in comparison to TODGA solvents, as efficient back extraction in TODGA systems was possible only under pH conditions (i.e. acid concentration below 0.1 M), where the aqueous phase needed to
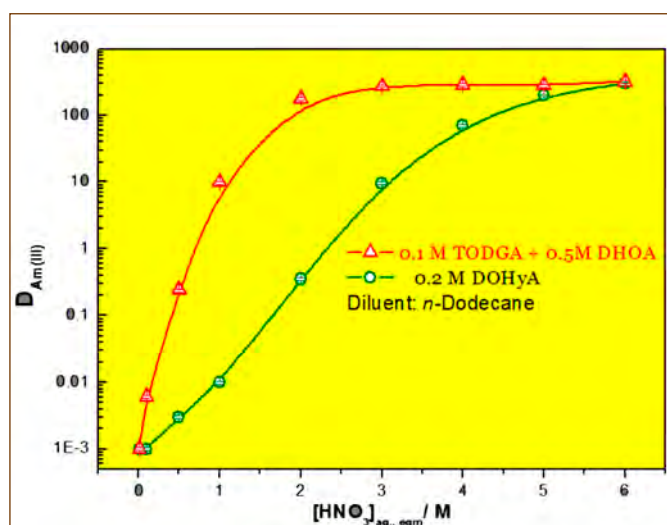

Figure 3: Comparison of the distribution ratio of Am(III) for TODGA and DOHyA at different nitric acid concentrations
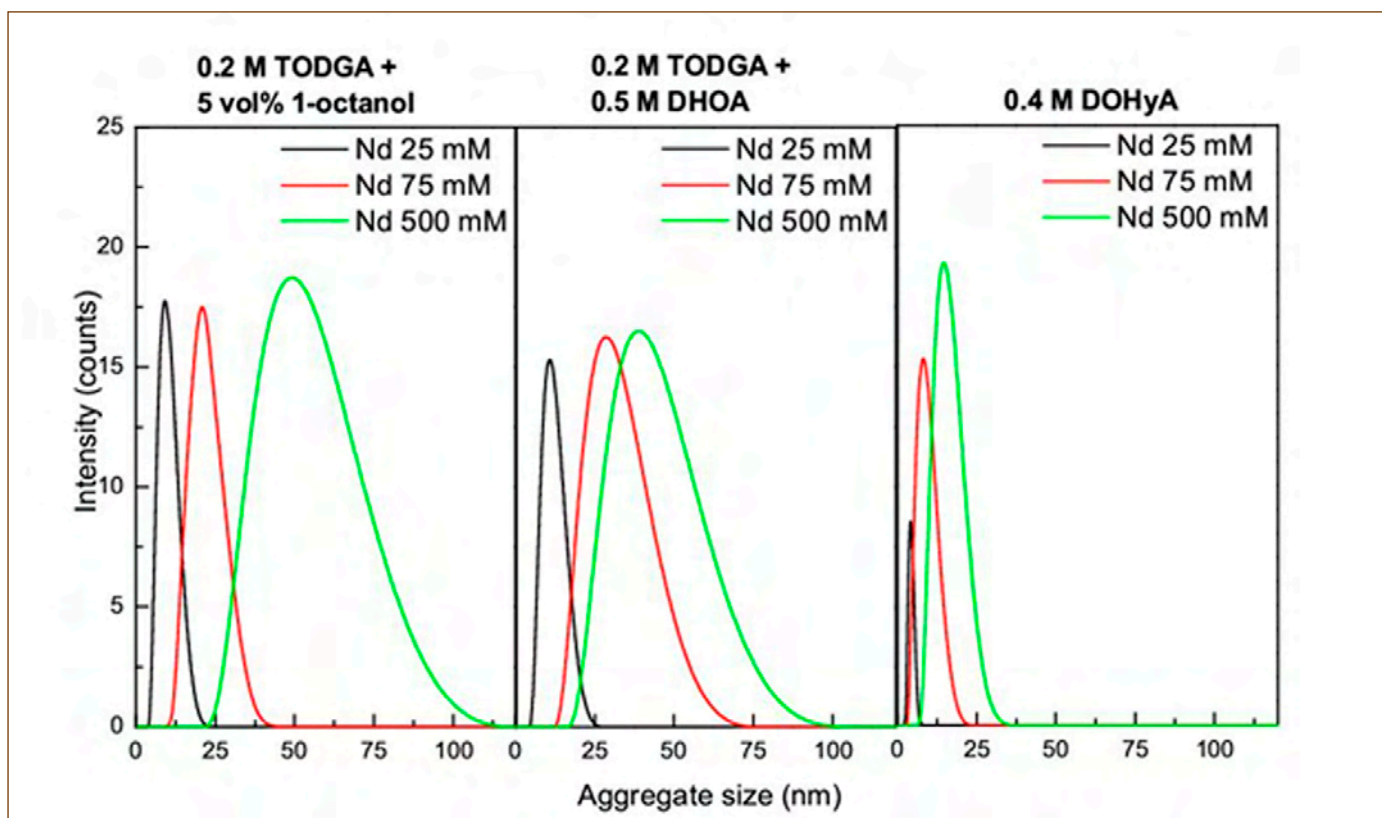
Figure 4: Temperature of ejected sodium Aggregate size distribution curves from dynamic light scattering measurements for two different TODGA solvents and DOHyA solvent under similar Nd(III) loading conditions

be stabilized by buffering agents. Thus, the results of preliminary studies on Am(III) distribution from nitric acid medium showed that DOHyA is a better extractant in comparison to TODGA for the treatment of high level waste solutions.

The aggregation behavior of DOHyA in comparison to TODGA was probed by dynamic light scattering studies. The average sizes of reverse micellar aggregates under similar extraction conditions were measured for different TODGA solvents and DOHyA (see Figure 4). The aggregate sizes in DOHyA were always smaller and there was only a minimal increase in aggregate size with increase in loading of the organic phase. Probably, the smaller size of the molecule and a smaller number of polar groups prevented the excessive aggregation of DOHyA, effectively avoiding the third phase formation. It should be emphasized here that the extraction of the prototype trivalent metal ion, Nd(III) was similar in both the solvents, though the average aggregate sizes in DOHyA was much smaller than TODGA.

Studies using simulated waste solution

HLLW is a complex mixture of several fission products, corrosion products and activation products resulting from the reactor operation. When a novel extractant is proposed for the partitioning of minor actinides from HLLW, it is necessary to study the co-extraction of other metal ions in this solvent. The extraction

and stripping of metal ions from a fast-reactor simulated high-level liquid waste (FR-SHLLW) using 0.4 M DOHyA/ n-dodecane solvent was studied in a 20-stage mixer-settler housed in a radioactive glove box (Figure 5). The FR-SHLLW was spiked with Am(III) and Eu(III) tracers. Quantitative extraction of all the trivalent metal ions with minimal co-extraction of other fission products was observed in 3-4 stages of mixer-settler operation, without any phase separation problems. Also, quantitative back extraction using 0.5 M nitric acid was achieved in three stages, indicating total separation of alpha activity from the feed solution in easy steps using DOHyA in comparison to the other proposed solvents.

The hydrolytic and radiolytic stability of the ligand are two important criteria for the selection of novel extractants for treatment of highly radioactive solutions. The solvent phase containing DOHyA retained the extraction and back-extraction performance after static gamma irradiation up to absorbed dose of 200 kGy. This showed that the ligand can efficiently withstand the radiation field under the process conditions. Similar to the diglycolamides, the hydrolytic degradation of DOHyA was negligible, after keeping in contact with 4 M nitric acid for weeks. The suitability of DOHyA for process scale applications of HLLW treatment was confirmed in the above studies.
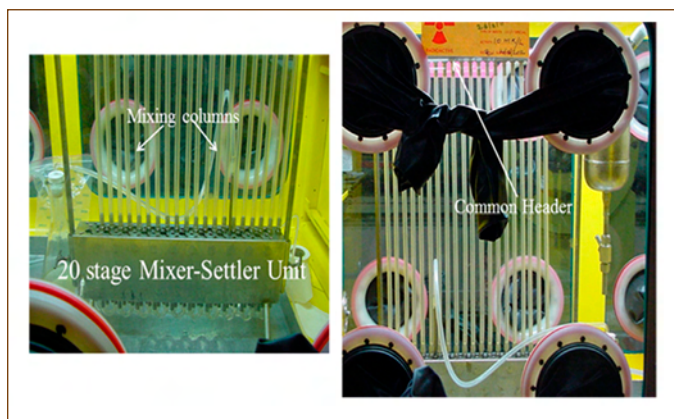
Figure 5: Photograph of the 20-stage mixer-settler facility in glove-box for counter-current extraction and stripping studies

Treatment of HLLW from metallic fuels

U-Pu-Zr based metallic fuels contain minimum 6 wt.% of zirconium as a constituent element of the fuel. Dissolution of spent metallic fuels in nitric acid medium followed by aqueous reprocessing using advanced PUREX reagents has been actively studied in MC&MFCG. It was found that nearly 60% of zirconium in the fuel gets into the dissolver solution, while dissolving with hot concentrated nitric acid containing traces of hydrofluoric acid. After the uranium and plutonium of spent metallic fuel solution is separated in the advanced PUREX cycles, the remaining high-level waste solutions retain major part of the zirconium from the fuel. It is estimated that the amount of zirconium in HLLW arising from spent metallic fuels could vary from 6 g/L to 8 g/L, while the total concentration of all the trivalent metals in HLLW would be ~ 3 g/L.

The aqueous chemistry of zirconium is rather complex. The extensive hydrolysis of zirconium results in the formation of a variety of polymerized species of $[Zr_n(OH)_x(H_2O)_y]$ in aqueous solutions, depending on the acidity. It has been observed that the polymerization and precipitation tendency of zirconium is enhanced at high concentrations and low aqueous phase acidities, often leading to interfacial crud formations during solvent extraction processes involving zirconium. The treatment of HLLW solutions containing significant quantities of zirconium would, therefore require extractants and processes different from those used for the treatment of conventional fuel solutions. Our recent studies showed that many of the diglycolamide solvents

proposed for minor actinide partitioning were not suitable for the treatment of HLLW solutions with Zr(IV) concentrations > 3 g/L. Therefore, a pre-treatment step for the selective removal of Zr(IV) would be essential during the treatment of HLLW solutions arising from metallic fuels.

A solvent system consisting of 0.4 M DOHyA / n-dodecane was found to extract Zr(IV) from nitric acid medium without any crud formation, when the concentration of Zr(IV) was up to 9 g/L. Therefore, selective extraction of Zr(IV) from FR-SHLLW was studied using this solvent, and all the Zr(IV) in FR-SHLLW was found to be preferentially extracted to this solvent in minimum number of extraction stages. The other metal ions loaded to the DOHyA solvent along with Zr(IV) in the extraction step could be recovered to the aqueous phase during the scrubbing stages using 0.5 M or 1 M nitric acid. The DOHyA solvent retained all the Zr(IV) and Mo(VI) from FR-SHLLW after this scrubbing step. The Zr(IV) in this solvent was then selectively stripped to the aqueous phase using an aqueous phase containing 0.2 M oxalic acid in 0.5 M nitric acid. When the Zr(IV) content of FR-SHLLW solution was increased, the extraction of all the metal ions other than Zr(IV) and Mo(VI) by the DOHyA solvent was observed to drop sequentially. The results showed the possibility of minimizing the co-extraction of other metal ions by using a stoichiometric concentration of DOHyA, which preferentially extracted Zr(IV) and Mo(VI). A higher loading of Zr(IV) in the DOHyA solvent reduced the loading of other metal ions as well as enhanced the scrubbing of other co-extracted metal ions using dilute nitric acid.

In summary, a novel extractant for the treatment of the HLLW solutions from nuclear reprocessing streams has been developed in our laboratory. DOHyA is an easy to synthesize extractant and does not pose third phase problems during solvent extraction processes. Along with this advantage, the extraction efficiency of DOHyA is as superior as other diglycolamide extractants. The higher extraction capacity and zirconium selectivity of the solvent makes it suitable for treatment of HLLW solutions from U-Pu-Zr based metallic fuels also.

Reported by
Dr. T. Prathibha and Colleagues
Materials Chemistry & Metal Fuel Cycle Group

Stability of B1-type Oxides in BCC Iron by Density Functional Theory Calculations

The residence time of the fuel subassembly and hence the achievable fuel burn up is limited by either the void swelling of the wrapper or creep strength of clad. Since fuel cycle cost is strongly linked with burn up, selection of materials resistant to void swelling and irradiation creep is very important. Austenitic stainless steels could not be employed for doses above 120 dpa as their void swelling is detrimental. Temper embrittlement in ferritic steels, associated with segregation of impurities to grain boundaries and consequent weakening, poses a serious limitation in its successful employment at low temperatures. Oxide dispersion strengthened (ODS) steels is an alternative with the advantage of ferritic martensitic steel with respect to high swelling resistance and the potential to push operating temperature to 923 K and beyond from creep strength consideration. The improved performance of ODS steel is related to the densely dispersed fine oxide particles hindering dislocation mobility and trapping point defects produced by irradiation. It is imperative that these oxide particles are retained during thermal processing and service. Characterization of these oxide particles, including their crystal structure and composition, is an active research field since different phases and chemical variants of a same structure respond differently to high temperatures and irradiation. A number of transmission electron microscopy studies show that these oxide nanoclusters in ODS steels are of $Y_2Ti_2O_7$ pyrochlores. Heavy ion irradiation studies show further that the average size of the oxide particles decrease dramatically and their population increases sharply with irradiation damage. These studies also show that the oxide dispersion observed after irradiation has no distinct lattice structure and they are not $Y_2Ti_2O_7$, Y_2TiO_5 or Y_2O_3.

Other studies, including an article in Nature Materials, on the other hand, asserts that the oxide nanoclusters in ODS steel are defective TiO particles with NaCl (B1-type) structure. The chemical composition and structure of the oxide dispersions have actually been a matter of debate. Some studies have reported that these oxide particles lack an identifiable crystal structure. An atom probe tomography characterization of the chemistry of the nanoclusters in ODS steels have determined YO, TiO and O_2 clusters with a mean composition of $YTiO_2$, unrelated to any stoichiometric compound. These studies thus indicate that the B1-type TiO is also a likely dispersion in these steels. This view is further supported by several studies on improving the properties of ODS steels where B1-type oxides (MgO, CaO, BaO, SrO) have been included in the investigation of their ability to trap He in the iron matrix, influence on mechanical and micro structural properties and resistance to irradiation. Studies also exist investigating the precipitation of different oxides and their

strengthening mechanisms in ODS steels. However, the list of oxides to be investigated as dispersion in ODS steels have not been well established. Despite this, no study has directly investigated the stability of B1-type oxides in BCC iron.

In view of this and in order to gain comprehensive insight on the structure and stability of the B1-type oxide dispersions, the formation energy of 31 different B1-type oxides in bcc iron and the bulk moduli of the oxide embedded iron matrix have been computed. These B1-type oxides will be referred as MO oxides with M substituted by the 31 different elements. This work show that oxides, such as, TaO, MnO, AlO, SiO, ZrO, ScO, ZnO, MgO and SnO constitute stable oxides in the iron matrix, which tend to retain the bulk modulus of the iron matrix. Whereas, oxides, such as, TiO, VO, CrO, FeO, CoO, NiO, MoO, RuO, RhO, HfO, WO, ReO, OsO, and IrO are chemically less stable in the iron matrix though its bulk modulus is retained. This work, through comparison of formation energies of the oxides in the iron matrix, shows also that YO dispersion will be more stable against dissolution than $Y_2Ti_2O_7$ particles in ODS ferritic steels.

The B1-type oxides embedded in iron is modelled by placing an M_4O_4 cluster in a 4x4x4 BCC Fe supercell with 128 sites. This M_4O_4 cluster is created by replacing 2 nearest neighbour Fe atoms with 2 M atoms each on two adjacent (110) planes and by placing an O atom at the nearest octahedral interstitial sites to each of the 4 M atoms. The pair of M atoms on the given (110) plane is rotated by 90° with respect to the other pair on the adjacent (110) plane. When these 4 M and 4 O atoms are linked, they form a simple tetragonal cell resembling the simple cubic cell with 4 Na and 4 Cl atoms placed alternatively at its corners constituting one eighth of the conventional B1-type NaCl unit cell. This is illustrated in Figure 1. Thus the M_4O_4 unit is placed in the BCC Fe supercell such that the M's substitute for Fe and O's
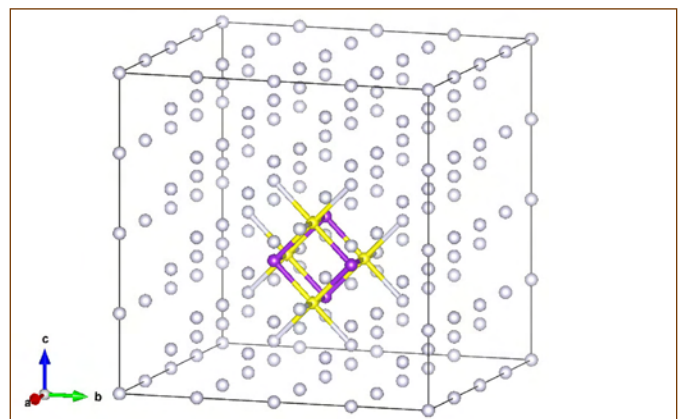

Figure 1: Supercell model of the B1-type MO oxide in BCC iron. M atoms are in blue and O atoms are in yellow colours
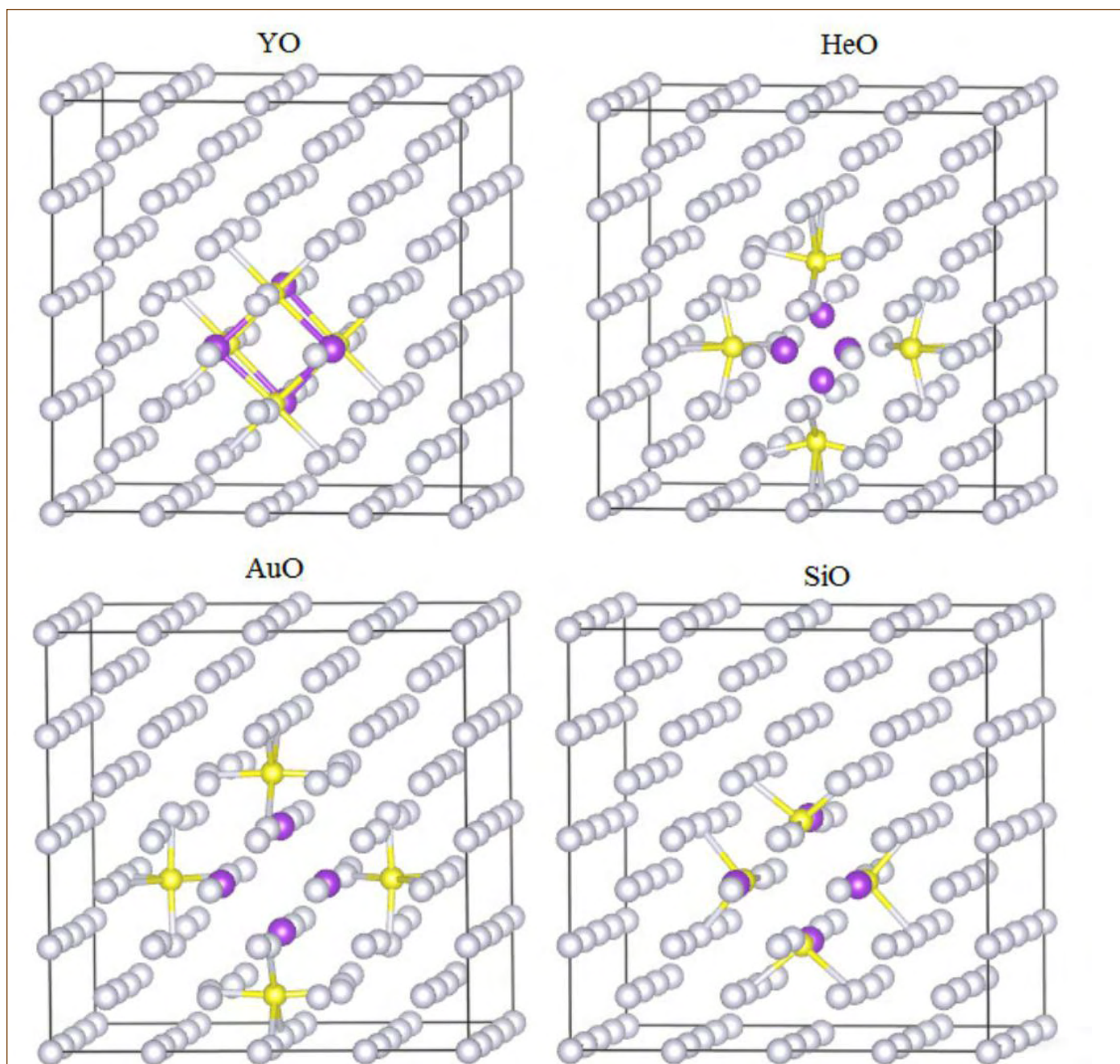
Figure 2: Relaxed structure of Fe supercell with embedded M_4O_4 B1-type oxides depicting 4 different patterns of relaxations of the oxide clusters. Structure with label YO represents the relaxation pattern where M_4O_4 unit remains intact. Majority of MO belong to this category

occupy the associated octahedral interstitial sites in the same manner as all Cl atoms occupy the octahedral holes in the BCC Na to give the B1-type NaCl crystal structure. This work considers 31 different elements for M (AlO, AuO, BaO, CaO, CdO, CoO, CrO, CuO, FeO, HeO, HfO, IrO, MgO, MnO, MoO, NbO, NiO, OsO, ReO, RhO, ScO, SiO, SnO, SrO, TaO, TiO, VO, WO, YO, ZnO, ZrO).

The formation energy (E^f) of the M_4O_4 oxide in the bulk BCC iron is calculated from the expression: E^f $(M_4O_4)=E(Fe_{124} M_4O_4)-$ $124/128$ $E(Fe_{128})-E(M_4O_4)$ where $E(Fe_{124}M_4O_4)$ and $E(Fe_{128})$ are respectively the total energies of the supercells containing the oxide cluster M_4O_4 and pure BCC Fe. $E(M_4O_4)$ is the total energy of the free M_4O_4 cluster. The formation energy in this work thus represents the energy related to dissolving M_4O_4 as a single entity in the BCC iron matrix. It is similar to the formation energy of elemental solutes in a crystal. It does not represent dissolving M_4O_4 unit into elemental M's and O's in the iron matrix. Positive formation energy represents endothermic reaction of M_4O_4 with Fe matrix while negative formation energy represents exothermic reaction. The Vienna Ab initio Simulation Package (VASP) was used for the calculation of the total energies required in the formation energy calculations. See Mater. Today Commun.

25, 101266 (2020) for more information. Besides formation energies, the bulk moduli of the oxide embedded iron have also been calculated by fitting their E (V) data to the Vinet equation of state.

Before analyzing the structure of the M_4O_4 clusters placed in the iron matrix, their relaxed structure were examined without the iron matrix. It is found that the relaxed free M_4O_4 clusters remain intact as a single entity though distorted relative to the initial cubic form. The free He_4O_4 and Os_4O_4 clusters are not intact. The He_4O_4 cluster relaxes into two O_2 clusters and 4 isolated He atoms. The Os_4O_4 cluster relaxes to Os_2O_4 and two isolated Os atoms.

In the initial cubic cluster, M-M and O-O bond lengths are same. Therefore, the difference between the M-M and O-O relaxed bond lengths are an indication of the distortion of the M_4O_4 clusters from the cubic form. Comparison of the differences between M-M and O-O bonds shows that majority of the O-O bonds are expanded relative to the M-M bonds.

The structures of all the $Fe_{124}M_4O_4$ systems were then examined. The positions of M, O and the surrounding Fe atoms and the associated bond lengths are found modified in the relaxed systems. The relaxed supercells remain cubic for most systems with a small deviation within 3%. This deviation from cubic form is slightly higher than 3% for Sr_4O_4 and Y_4O_4 embedded supercells. The conclusions of this analysis are (i) majority of the M_4O_4 units remain intact with M and O atoms bonded as in the beginning of the structural optimization. He_4O_4, Au_4O_4 and Si_4O_4 are exceptions. In the former two systems (ii and iii), He and Au atoms stay close to their respective substitutional positions whereas the O atoms detach from He and Au atoms and attach with neighbouring Fe atoms. Correspondingly, these Fe-O bond lengths are relatively shorter in these systems. Further, while the O atoms from He4O4 are still located near their original octahedral interstitial sites after relaxation, the O atoms from Au_4O_4 are relaxed to the next tetrahedral interstitial sites. O atoms detaching from He and Au atoms and attaching with neighbouring Fe atoms may be understood as follows: Noble elements He and Au with negligible reaction with O atoms allow them to leave, Fe atoms react readily with O atoms to produce Fe-O oxides hence attachment with Fe atoms. Si_4O_4 (iv) relaxes to four SiO pairs, located approximately at their respective initial positions. This is because the differences between the first and second nearest neighbour Si-O and O-O bond lengths have become larger than the initial lengths. These four different patterns of relaxation (YO, HeO, Au, SiO) are shown in Figure 2. Majority of the MO clusters including MgO, AlO, TiO, MnO, NiO, YO, ZrO and HfO remain intact as M_4O_4 units in Fe matrix with some amount of distortion from the cubic form. Analysis of relaxed bond lengths further shows that the Fe matrix surrounding the M_4O_4 clusters is expanded.

Through the energies of 4 distinct Y_2O_3-Fe interfaces, the mechanism of resistance to irradiation damage of Y_2O_3 dispersion strengthened steels has been studied. These interfaces act as strong traps for both interstitial and vacancy defects, facilitating recombination without altering the interface structure.

This catalytic elimination of defects is considered to be the mechanism behind the improved performance of ODS steels with respect to irradiation creep and swelling. The work presented here shows that the degree of distortion of the M_4O_4 clusters embedded in the iron matrix span over a range. Thus, it will be interesting to investigate the Helium trapping capability of these oxide-iron interfaces.

The formation energies of the oxides in the iron matrix are related to their ability to resist the motion of dislocations in the iron matrix. Endothermic interaction between the oxide particles and the iron matrix is considered to keep the oxide particles undissolved in the iron matrix. Undissolved oxide particles are more effective to pin dislocations. Figure 3 shows the formation energies of oxides in the iron matrix as a function of relaxed volume of each of the 31 MO embedded iron systems. It is evident from the figure that the oxides such as BaO, SrO, YO, CaO, SnO, CdO, ZrO, ScO, MgO, ZnO, SiO, AlO, MnO and TaO with endothermic formation energies, are potential oxides to remain intact in the Fe matrix. It is further evident that the oxides such as IrO, HfO, WO, NbO, RhO, ReO, MoO, OsO, TiO, CoO, VO, CrO, NiO, CuO and FeO are less stable in the iron matrix since their exothermic formation energies are manifestation of reaction between MO and Fe where exchange of M for Fe or nucleation of M-Fe-O oxide is favourable. The endothermic formation energy of MgO and the exothermic formation energy of TiO are similar to their reported interface energy with iron matrix. It is also found that some of these exothermic oxides such as HfO, WO, MoO and ReO remain intact though they are not observed experimentally. This is likely
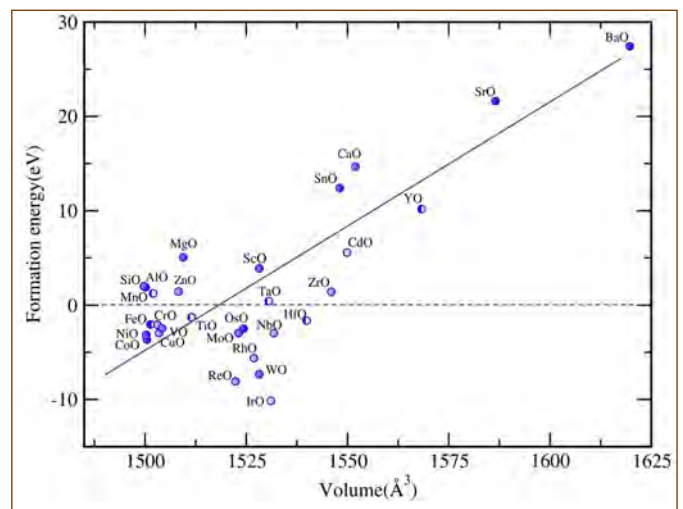

Figure 3: Formation energy of B1-type oxides in BCC iron versus volume of the oxide embedded BCC iron. The lines are guides to eye
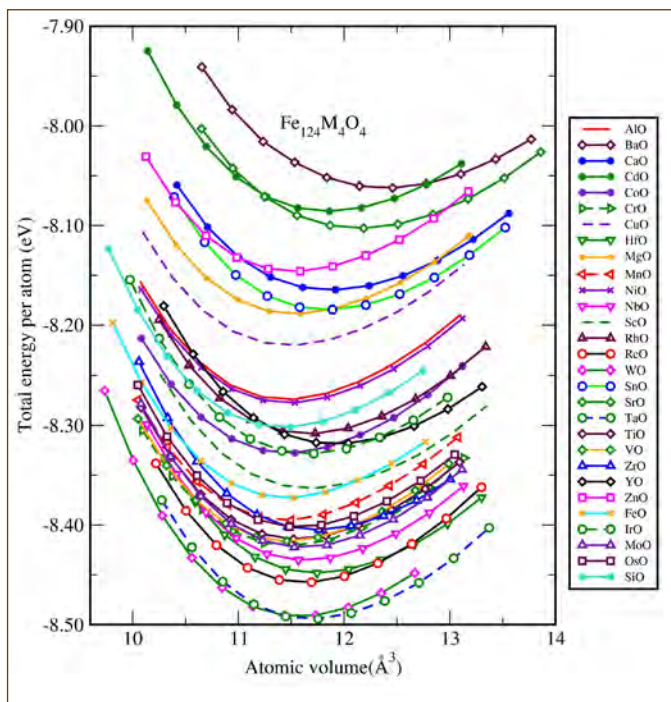
Figure 4: E (V) equation of state for B1-type oxide embedded BCC iron supercells (Fe$_{124}$M$_4$O$_4$)

because the iron matrix enhances the M-O bonding in these oxides. The other oxides such as NiO, NbO, TiO, VO, CoO and CuO which are observed experimentally, are calculated to have exothermic formation energies. This may be because the transition metals Ni, Nb, Ti, V, Co and Cu bond appreciably with the surrounding Fe as is evident from their intermetallic phases. Elements such as Zr, Cd, Y, Sr and Ba have large endothermic formation energies in BCC iron consequently their oxides (with endothermic formation energy) are highly stable in the iron matrix. It may be noted that HeO and AuO don't stay intact in the iron matrix. But note that,
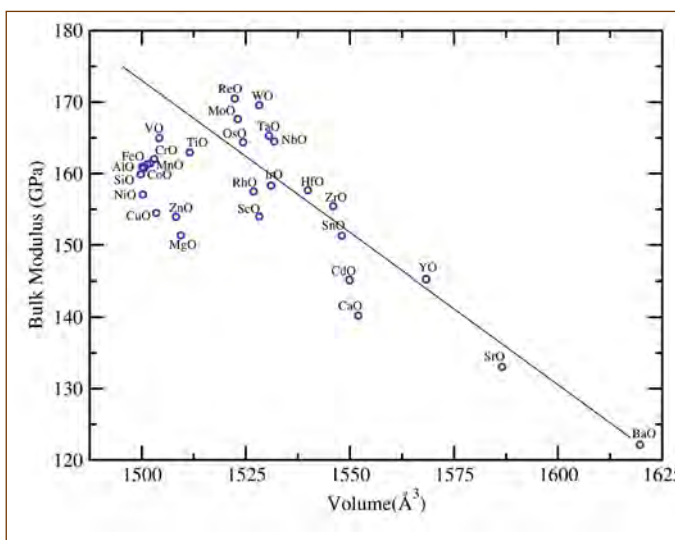
in ODS steel under irradiation, O and He atoms are very likely to encounter each other. This work suggests that the tendency of O to trap He or vice versa is weak.

Another observation from this Figure 3 is that the formation energies exhibit a correlation with the radius of the M atoms of the oxides when we consider BaO, SrO, YO, HfO, ZrO, TaO, CaO, NbO, WO, MoO, ScO, OsO, TiO, VO and FeO. Oxides such as MgO, SiO, MnO and IrO show appreciable deviation from this relation. It will be shown latter that the oxides that deviate from this correlation are those in which the hybridization between the valence orbitals of M and Fe are either weak or strong relative to those in other oxides.

The bulk modulus is a measure of the ability of a substance to withstand changes in its volume by compression. The bulk modulus is related inversely to the thermal expansion coefficient of solids. Thus the bulk modulus of oxide embedded iron will be a useful indicator to identify the oxides for ODS steel that resist compression or expansion. Therefore the bulk modulus of all the 31 oxide embedded iron systems were computed by fitting their E(V) data to the Vinet equation of state. Figure 4 shows the E (V) equation of state for all these systems. Smooth curves indicate that VASP gives E(V) for Fe$_{12}$4M$_4$O$_4$ supercell systems in the same manner as it gives for element and compound crystals. It is found that the relaxed equilibrium volumes of all the systems, obtained by fitting the E(V) in Figure 4, are increased with reference to pure Fe. This increase in volume is generally from 3 to 5% except for CaO, SrO, BaO, YO, ZrO, HfO, CdO, and SnO embedded systems for them the increase is between 5 to 11%. Estimates of volumes of M$_4$O$_4$ from their respective atom sizes show that the increase in the volumes of the supercells are generally more than that contributed by M$_4$O$_4$ units.

Figure 5: Bulk modulus versus relaxed equilibrium volumes of oxide embedded BCC iron. The line is a guide to eye.
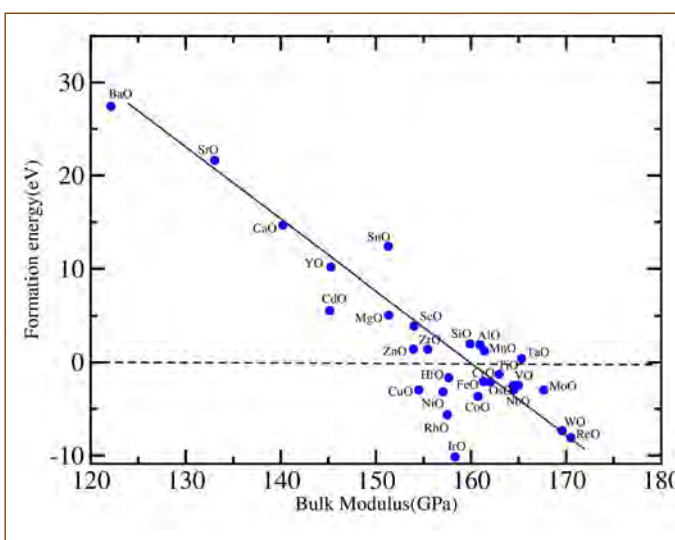

Figure 6: Formation energy of B1-type oxides in BCC Fe versus bulk modulus of the oxide embedded BCC iron. The lines are guides to eye.

It is further found that the bulk modulus of oxide embedded iron is generally reduced compared to the bulk modulus of pure iron (185 GPa). This reduction in bulk modulus correlates with the increase in the equilibrium volumes of the oxide embedded iron as can be seen in Figure 5. The reduction in bulk modulus of BCC iron due to the oxide particles appears to be in agreement with the reduction in bulk modulus and increase in lattice parameters of BCC iron with alloying elements Al, Si, V, Cr, Mn, Co, Ni and Rh as well as with the reduction in bulk modulus of BCC iron with embedded $A_2B_2O_7$ oxide particles. It is evident from Figure 5 that the oxides such as CaO, SrO and BaO, with relatively higher contribution to equilibrium volumes, have reduced the bulk modulus of BCC iron appreciably. The reduction in the bulk moduli of oxide embedded iron with the associated increase in the volumes compared to pure iron is further in accordance with the reported reduction in melting point and density of ODS steels compared to pure iron. Compared to ScO embedded iron the bulk modulus of WO embedded iron is appreciably higher though their volumes are comparable. Correspondingly, it is found that the Fe-W bond length (2.32 Å) are shorter than Fe-Sc bond lengths (2.48 Å) indicating that the Fe-W bonding is strong relatively.

As stated earlier, ODS steels with higher bulk moduli and endothermic formation energies for the dispersed oxide particles are able to resist thermal expansion and dislocation motion leading to stable microstructure at elevated temperatures. In this connection, the formation energy of oxide dispersions in BCC iron is plotted against the bulk moduli of the oxide embedded BCC iron. This is shown in Figure 6. It is evident from this figure that ZrO, AlO, SiO, MnO and TaO have endothermic formation energies with relatively higher bulk moduli for respective oxide embedded BCC iron, making them suitable candidates as dispersions in ODS iron alloys. It is also evident that oxides such as YO, CdO, SnO, MgO, ZnO and ScO constitute stable oxides in the iron matrix though they cause a reduction of the bulk modulus. The other oxides, such as, TiO, VO, CrO, FeO, CoO, NiO, MoO, RhO, HfO, WO, ReO, OsO and IrO retain or enhance the bulk modulus of the iron matrix, but their exothermic formation energies indicate that they are chemically less stable. This work thus shows that TiO stays intact in the BCC iron matrix but it is not the most stable oxide. Figure 6 further shows that the formation energies of the oxide particles have a correlation with the bulk modulus of the respective oxide embedded iron. It can also be seen that CaO, SrO and BaO are quite stable against dissolution but they cause considerable reduction of the bulk modulus of the iron matrix. Comparison of the formation energies of YO and $Y_2Ti_2O_7$ oxides in the iron matrix from literature show that YO dispersion is more stable against dissolution then $Y_2Ti_2O_7$.

It is evident that most of the oxides predicted to be stable in the iron matrix (except AlO and TaO) are observed experimentally whereas many of the oxides which are unstable in the iron matrix are not observed experimentally (AuO, CrO, HfO, IrO, MoO, OsO, ReO, RhO, WO. Note that Hf-O precipitates with Hf:O ratio close to 1 has been reported in Fe14Cr0.22Hf alloy fabricated by spark plasma sintering). Inspection of iron-binary phase diagrams show further that the majority of the M's of the exothermic MO oxides (Ir, Rh, Ni, Co, Cr, V, Mo, Nb, Re) form extended solid solution with Fe unlike M's of endothermic oxides (Ca, Sr, Ba, Y, Cd, Sn, Mg, Sc, Zr, Mn, Ta).

As mentioned earlier, the oxides with endothermic formation energies, which tend to retain the bulk modulus of the iron matrix, are potential candidates for the development of improved ODS steels. Comparison of bulk moduli of the MO embedded iron with those of the $A_2B_2O_7$ embedded iron indicates that the MO oxides are better candidates to retain/improve the bulk modulus of the iron matrix. Thus the MO oxides, such as, SnO, MgO, YO, CdO, ScO, ZrO, AlO, SiO, MnO, TaO and ZnO, are predicted to be suitable candidates to be investigated as dispersion in ferritic matrix. Among these oxides, MgO has been already studied as an alternative dispersion in ODS steels.

The formation energies of the dispersions are found to be endothermic for some oxides and exothermic for other oxides. Since these formation energies are manifestation of bonding between Fe, M and O atoms, the projected electronic density of states of the oxide embedded iron were analyzed to gain more insight into the origin of the exothermic and endothermic formation energies. The projected density of states of s or d electrons of M, d electrons of nearest Fe and the p electrons of O atoms are plotted in Figure 7. It is evident that the p density of states are placed almost over the same energy range with similar hybridization with the Fe and M density of states whereas the s or d density of states from M's exhibit distinguishable degrees of overlap with the d density of states from nearest Fe. That is, the M's with exothermic formation energy for MO, such as NiO, RhO and IrO, exhibit strong overlap with the Fe d density of states while the M's with endothermic formation energy for MO, such as MgO, YO and ZrO, exhibit weak overlap with the Fe density of states. It is also evident from (a), (b) and (c) panels of Figure 7 that the hybridization between Mg-s and Fe-d is negligible compared to that between Y-d and Fe-d, and between Zr-d and Fe-d states. This leads to relatively large positive formation energy for MgO, which makes it to deviate from the correlation between the formation energy and volume in Figure 3. Looking at the DOS in the (d), (e) and (f) panels of Figure 7, it can be seen that the hybridization between Ir-d and Fe-d over -6 to 0 eV is strong compared to that between Ni-d and Fe-d, and between Rh-d and Fe-d (Ir-d band width and the area under Ir-d occupied DOS are more comparable to those in Ni-d and Rh-d DOS.) This strong hybridization between Ir and Fe states leads to relatively large exothermic formation energy for IrO in the iron matrix, causing
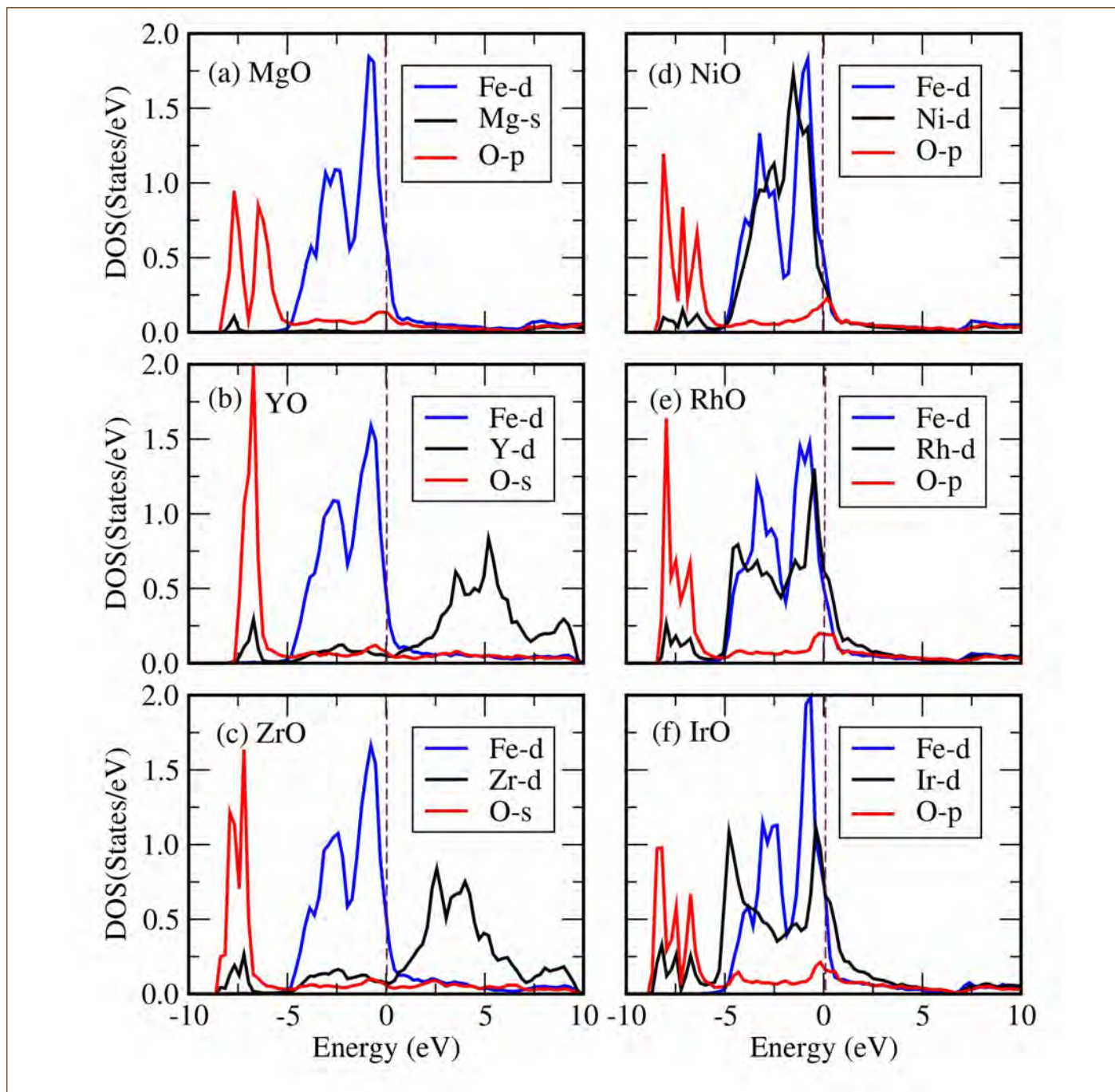
Figure 7: Projected electronic density of states from (a) MgO, (b) YO, (c) ZrO, (d) NiO, (e) RhO and (f) IrO embedded BCC iron. Vertical lines at 0 eV are Fermi levels.

its deviation from the correlation in Figure 3. That is, most of the MO's derive their mechanism for the endothermic or exothermic formation energies from the degree of overlap between valence electron density of states from M and Fe atoms.

The main conclusions from this work are that oxides, namely YO, CdO, SnO, MgO, ScO, ZrO, SiO, AlO, MnO, TaO and ZnO with endothermic formation energy in the iron matrix combined with better bulk moduli, have the potential to improve the properties of ODS steels. B1-type MO oxides retain/improve the bulk modulus

of iron matrix better compared to $A_2B_2O_7$ pyrochlores. AlO, CrO, MoO, TaO, WO and ReO dispersions are predicted to enhance the bulk moduli of the iron matrix and remain structurally intact though they are not observed experimentally. This indicates that the iron matrix confine these oxides to remain intact.

Reported by
Chinnappan Ravi and his Colleagues
Materials Science Group

Young Researcher's Forum

Mrs. Geetisubhra Jena is working as a senior research scholar in CSTD. After acquiring M.Sc. Chemistry from Ravenshaw University, Odisha, she joined IGCAR in 2015 as a JRF. She registered for PhD in HBNI under the guidance of Dr. John Philip. Her thesis is titled "Development of graphene oxide based composite coating with improved corrosion resistance and antibacterial properties". She has authored 09 journal publications, attended 05 conferences and received two Best Poster Awards.

Fabrication of Graphene Oxide-nano SiO$_2$-Polydimethylsiloxane Composite Coating on Carbon Steel

Carbon steel (CS) is a widely used engineering material for marine structures, nuclear/fossil power plants, chemical processing industries, oil and water pipeline utilities due to its good strength, forming and welding abilities, easy availability, and low costs. Though uncoated CS performs well in dry environments, they undergo severe aqueous corrosion and microbial induced corrosion (MIC) in marine environments. To improve the corrosion resistance, anti-biofouling property, and its service life, surface modification techniques are widely used. Polymer composite coatings incorporated with corrosion inhibitors and biocides are broadly adapted for surface modification due to ease application, durability and cost effectiveness. Polydimethylsiloxane (PDMS) has unique physiochemical properties such as the low surface energy, low elastic modulus, high gas impermeability, heat/weather resistance, oxidation resistance, chemical inertness, corrosion resistance and anti-biofouling activities. However, mechanical properties of PDMS coating is a concern when it comes to practical applications.

Though there are many studies on anticorrosive and anti-biofouling properties of PDMS based coating, studies on composite coatings on corrosion resistance property and anti-biofouling property are scarce. This study is aimed at improving the mechanical robustness of PDMS coating by providing an interlayer of GO-nano-SiO$_2$ using anodic electrophoretic deposition (aEPD) for marine applications. GO and nano- SiO$_2$ are used to prevent the permeation of chloride ions and galvanic coupling between the GO and metal surface, respectively. From the experimental results, the mechanism of the corrosion resistance and anti-biofouling property of the new coating is elucidated. Further, biofilm formation on the coating is also studied systematically.

The carbon steel (CS) sheet with a thickness of 6 mm was cut into 40 mm × 20 mm specimens for this study. Using a modified Hummer's approach, GO nanosheets were prepared. To prepare the GO-nano-SiO$_2$ colloid, 0.1 wt.% GO and 0.1 wt.% nano-SiO$_2$ were mixed in 10 % ethanol in distilled water and stirred for 2 h followed by ultrasonication for 1 h. Anodic electrophoretic deposition (aEPD) utilized a two-electrode cell arrangement with a DC power supply where pretreated carbon steel specimen is used as a working electrode and platinum foil as counter electrode, placed parallel to working electrode, at 10 mm distance. The coatings with GO-nano-SiO$_2$ colloid is designated as GS. GS coatings were allowed to dry for 24 h at 70 ºC in a hot air drying oven to avoid coating failure due to water condensation in the coating. PDMS solution was prepared along with its curing agent in a volume ratio of 10:1 in organic solvent tetrahydrofuran (THF) of 10 mL. In order to achieve a clear solution, it was stirred for 15 minutes. The GS specimens were dipped in the PDMS solution for 30 seconds and lifted up at a speed of 3 mm/sec using dip coating unit. The procedure was repeated twice and finally, the specimens were heat treated at 120 ºC for 5h in a hot air oven and this coating is designated as GSP. To evaluate the effect of GSP composite coating, the CS specimen was also coated with PDMS
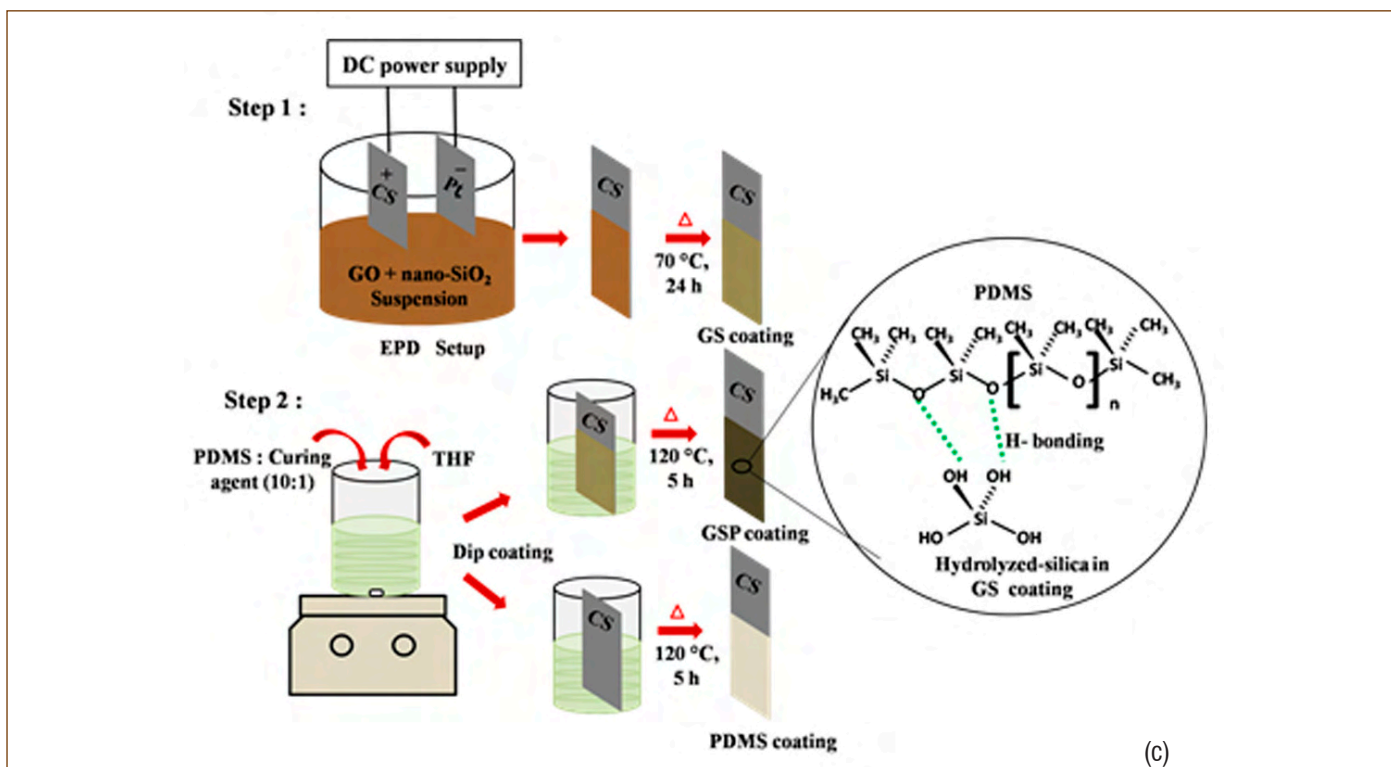
Figure 1: Schematic shows the process of preparing GO-nano-SiO$_2$ /PDMS composite coating.

of similar thickness and was designated as PDMS. A schematic representation of the preparation process of composite coating is shown in Figure 1.

The prepared coatings are characterized using Fourier transform infrared spectra (FTIR) and Laser Raman spectra (LRS), atomic force microscopy (AFM), field emission scanning electron microscopy (FESEM), energy dispersive X-ray spectroscopy (EDS), 3D measuring laser microscope and cross-hatch tape adhesion tester (ASTM D3359-02). The corrosion behavior of GS, PDMS, and GSP coatings along with uncoated specimen was studied by the electrochemical impedance spectroscopy (EIS) and potentiodynamic polarization method in 3.5 wt.% NaCl

solution using an electrochemical system. Galvanic corrosion test is done with uncoated specimen as one electrode and the coated specimens as the other electrode using the built-in zero-resistance ammeter (ZRA). To assess the quality of coatings, accelerated testing is done using the salt spray experiment as per ASTM B117-11. To investigate the anti-biofouling property of GS, PDMS, and GSP coated specimens; the coated specimens along with uncoated CS were exposed to Gram-negative *Pseudomonas* sp., which is a predominant biofilm former in sea water.

The Figure 2a shows the IR spectra for GS, PDMS, and GSP coating. The IR spectrum of GS film showed a small band between 3000 and 3600 cm^{-1}, corresponding to the stretching
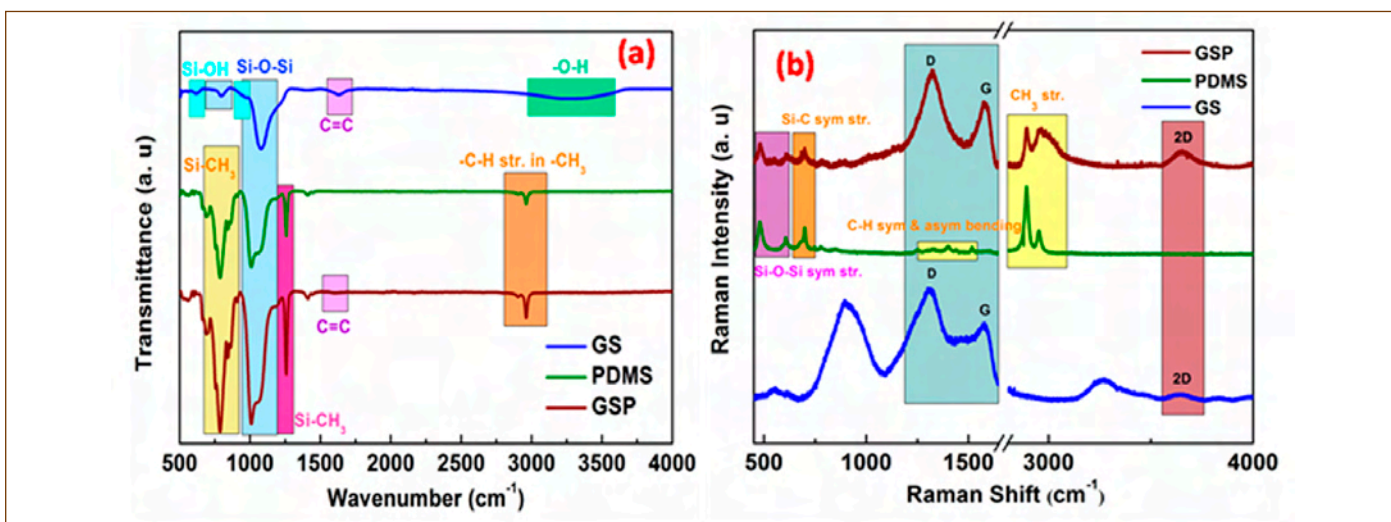

Figure 2: (a) ATR-FTIR spectra and (b) Raman spectra of as prepared GS, PDMS, and GSP composite coated CS specimens.

vibration of OH groups on the silica surface, which could be due to the formation of silanol groups (Si–OH) and the physisorbed water molecules from atmospheric air. The absorption peak observed at 1627 cm-1, is attributed to the stretching vibration of C=C present at the graphitic planes of GO. The intense and broad band at 950–1150 cm-1 attributed to the Si–O–Si asymmetric stretching appeared. FTIR spectrum of PDMS coated CS specimen exhibits absorption bands at 2960 cm-1 and 2905 cm-1, due to –C–H asymmetric stretching in Si–CH$_3$. The peak at 789 cm-1 corresponds to –C–H rocking vibration in Si–CH$_3$ and the peak at 1057 cm-1 corresponds to Si–O–Si stretching band. The GSP coated CS specimens showed similar peaks as PDMS coated CS specimen. Due to the high intensity peaks of PDMS, the peaks corresponding to GO were not discernible. However, a feeble peak at 1630 cm-1 indicates the C=C regime of GO confirmed the successful formation of GSP composite coating.

The Raman spectra for GS, PDMS, and GSP composite coated CS specimens are shown in Figure 2b. In the GS composite coated specimen, the characteristic D and G-bands were present at 1339 cm-1 and 1606 cm-1, respectively for GO. The in-plane E2g or vibration at the zone center of C=C conjugate bonds (G band) suggests the presence of defective sites in the hexagonal graphitic structure (D band). The value of ID/IG was found to be 1.27. The less intense and broad peaks of Si–O–Si regime were observed in GS coated specimens at 490–650 cm-1. These result showed that the as prepared PDMS film contains less water molecule absorbed with lower cross linking of Si–O–Si network. The presence of the distinct bands at 488 cm-1 and 613 cm-1 corresponding to Si–O–Si confirms the enhanced cross linking of Si–O–Si network in the presence of nano-SiO$_2$.

GO comprised of oxygen functional groups such as epoxide, hydroxide on the basal planes and carbonyl and carboxylic groups at the edges of the planes. Hence, the aqueous solution of GO has negative charges due to the dissociation of carboxylic groups to carboxylate (RCOO–) ions. Under the applied DC voltage during EPD, the negatively charged GO sheets migrate towards the anode i.e. the CS specimen. Once a DC voltage was applied to the aqueous GO suspension, water starts to electrolyze as Eq. 1.

$$2H_2O \rightarrow 4H^+ + 4e^- + O_2\uparrow \qquad (1)$$
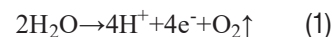
The (RCOO–) on GO sheets might interact with H$^+$ ions produced in water electrolysis and get neutralized and deposited on the surface of anode.

$$RCOO^- + H^+ \rightarrow RCOOH \qquad (2)$$
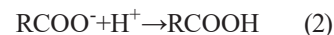
Another possible electrochemical reaction at the anode is as per Eq. (3-4), where the electrons move away from the GO planes, during the electric contact, thereby causing oxidation of RCOO–. The free migration of unpaired electrons leads to formation of covalent bond through dimerization of radicals (Eq. 4) as discussed in previous study [49].

$$2RCOO^- \rightarrow 2R^. + 2CO_2 + 2e^- \quad (3)$$

$$2R^. \rightarrow R\text{-}R \qquad (4)$$
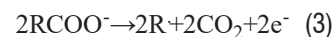
This Kolbe-like decarboxylation reaction can explain the loss of carboxylates and in our study, IR results also confirmed the partial reduction of carboxylic group present in GO during EPD. In the GS suspension, the hydrolyzed SiO$_2$ surface would adsorb H+ as pH of suspension is in acidic range ($\sim$ 3.4). The reactions involved above could be expressed as Eq. 5.

$$\equiv Si\text{-}OH + H^+ \leftrightarrow \equiv Si\text{-}OH_2^+ \qquad (5)$$
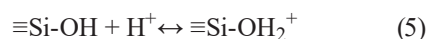
In addition, during EPD process, a significant amount of gas evolved is observed at the cathode surface. Therefore, the electrochemical reactions at cathode can be as Eq. 6.

$$2H_2O + 2e^- \rightarrow 2OH^- + H_2\uparrow \qquad (6)$$

Uniformity of the EPD deposited layer depends on the stability and dispersibility of the suspension during the deposition.

Figure 3a-c shows the 3D AFM micrographs of the GS, PDMS and GSP coated specimen, respectively. Figure 3a shows the typical ridges and ravine patterns due to the wrinkled morphology of GO and the RMS roughness of GS coated specimen was found to be 207 $\pm$ 8 nm, Figure 3b shows the morphology of PDMS coating where the RMS roughness was very low (5 $\pm$ 1 nm). Figure 3c shows the 3D AFM micrograph of GSP coating, which
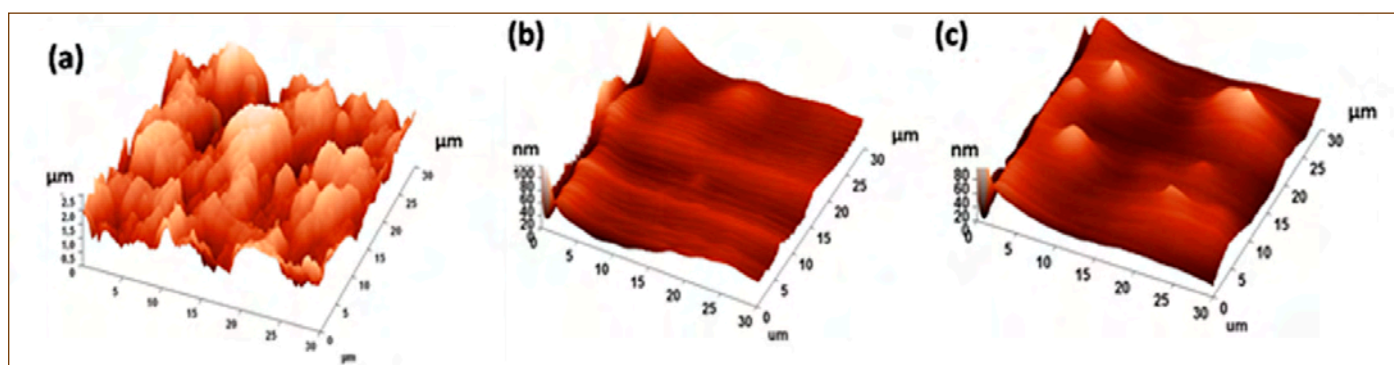

Figure 3: 3D AFM micrographs of as prepared (a) GS, (b) PDMS, and (c) GSP composite coated CS specimens.
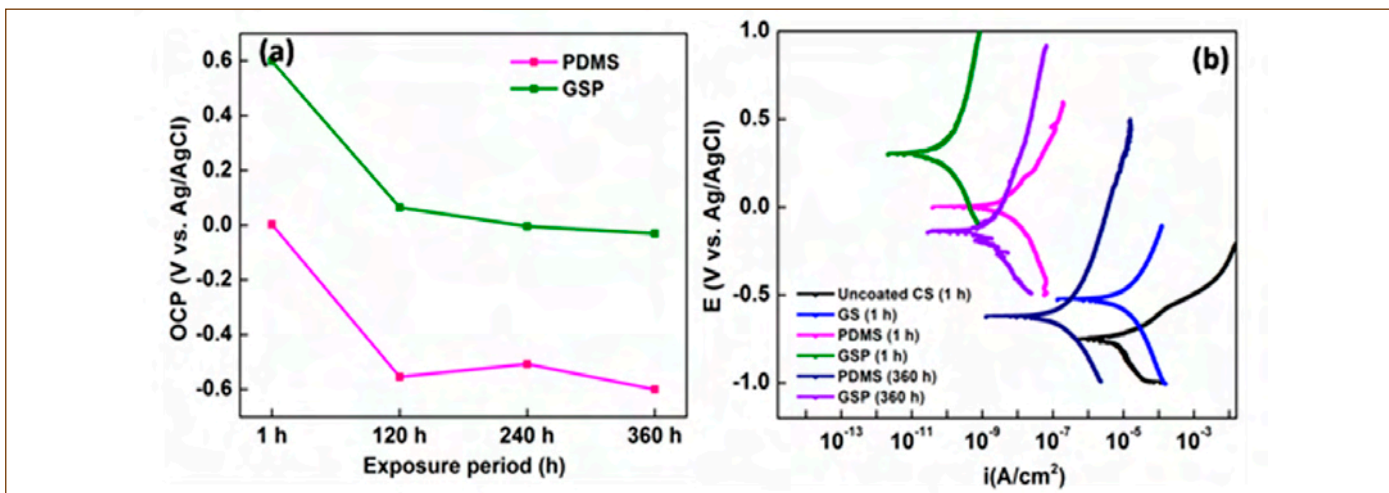
Figure 4: (a) Effect of immersion time on open circuit potential (OCP) of the PDMS and GSP coated CS specimens in 3.5 wt.% NaCl solution at 1 h, 120 h, 240 h, and 360 h, (b) Tafel plots of uncoated and coated CS specimens in 3.5 wt.% NaCl solution.

shows a smooth surface topography due the overlay of PDMS coating. The RMS roughness of the GSP coating was about 12 ± 1.1 nm, which was much lower compared to GS coatings, due to the PDMS overlay.

The corrosion protection of the coated specimen was studied by EIS. For long term corrosion protection performance, EIS analysis were done for PDMS and GSP coated specimen after immersion for 120 h, 240 h and 360 h in 3.5 wt.% NaCl solution. The electrochemical parameters extracted from the EIS plots of the uncoated and coated CS specimens are shown in Table 1.

Figure 4a shows the trends in the variation of OCP for PDMS and GSP coated CS specimens after 360 h immersion in chloride electrolyte (3.5 wt.% NaCl) at room temperature. Figure 4b depicts the polarization curves and the Tafel region extrapolation adapted

to derive the electrochemical parameters such as corrosion current density (i_{corr}), corrosion potential (E_{corr}), and polarization resistance (R_p). The uncoated CS specimen exhibits a narrow passive range and the corrosion current density increases quickly with increase in anodic polarization potential. GS exhibited a lower corrosion current density, higher polarization resistance, and ennoblement corrosion potential in comparison to the uncoated specimen. The polarization curve of the as prepared PDMS and GSP coating exhibited passive behavior in a much broader potential range and showed excellent ennoblement of around 700 to 800 mV in the E_{corr} values as compared to the uncoated CS. GSP coating showed the highest corrosion resistance with highest polarization resistance of 2.60×10^9 Ω.cm2, most positive corrosion potential and a five order less corrosion current density as compared to the uncoated CS, indicating its better
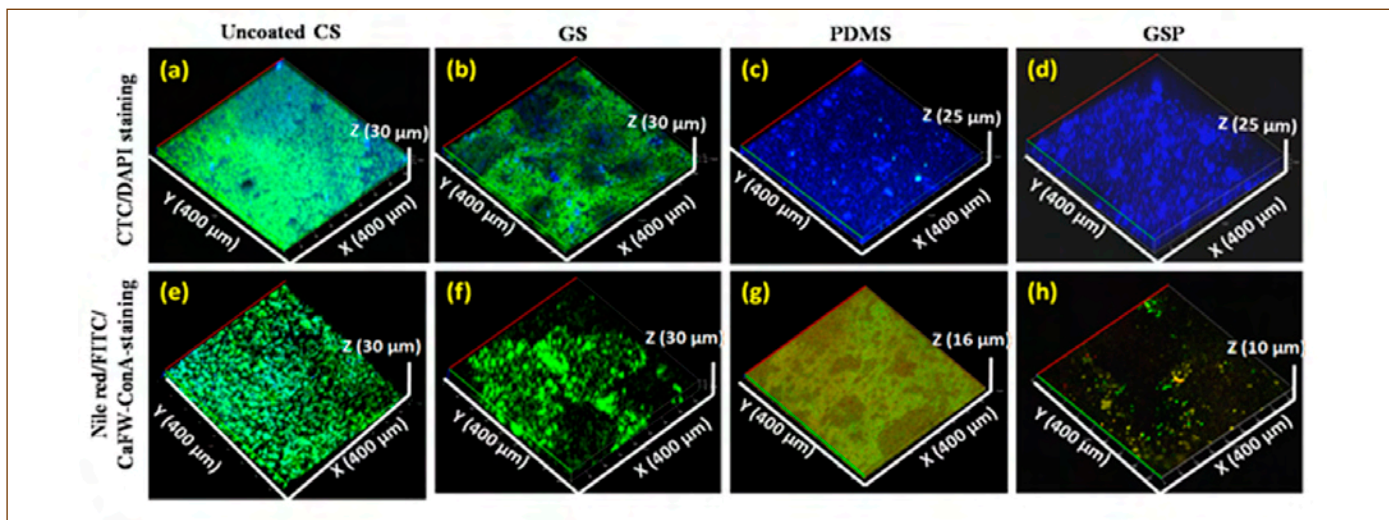

Figure 5 3D Confocal micrographs of CTC/DAPI stained (a) uncoated CS, (b) GS, (c) PDMS, (d) GSP coated specimen exposed to *Pseudomonas* sp. for 3 days. 3D Confocal micrographs of FITC/CaFW/ConA/Nile red stained (e) uncoated CS, (f) GS, (g) PDMS, (h) GSP coated specimen exposed to *Pseudomonas* sp. for 3 days.

Table 1 The electrochemical parameters extracted from modeling the EIS plots of the uncoated, coated (GS, PDMS, GSP) CS specimens for 1 h of exposure, and PDMS, GSP coated CS specimens for 360 h of exposure in 3.5 wt.% NaCl solution.										
Specimen Exposure period										
Circuit element	**Uncoated**	**GS**	**PDMS**				**GSP**			
	1h	1 h	1 h	120 h	240 h	360 h	1 h	120 h	240 h	360 h
R_{coat} (kΩ.cm^2)	-	0.08	106	0.98	11.05	12.4	47200	191	209	669
Q_{coat} (nMho. sn.cm^{-2})	-	3×10^6	4.7	258	41.2	28.5	0.02	2.28	1.31	0.84
n_{coat}	-	0.64	0.8	0.79	0.83	0.81	0.98	0.91	0.92	0.89
R_{ct} (MΩ.cm^2)	0.0016	0.0045	2.46	0.24	0.25	0.31	2330	10.9	13.9	46.8
Q_{dl} (nMho. sn.cm^{-2})	6.8×105	1.3×10^5	327	8990	9880	2090	1.88	429	370	234
n_{dl}	0.8	0.78	0.57	0.46	0.46	0.48	0.64	0.48	0.43	0.43
R_{diff} (kΩ.cm^2)	-	-	-	9.23	15.7	25.8	-	-	-	-
Q_{diff} (nMho. sn.cm^{-2})	-	-	-	285	42	27.8	-	-	-	-
n_{diff}	-	-	-	0.51	0.61	0.78	-	-	-	-
χ^2 ($\times 10^{-3}$)	8	2	3	0.3	0.6	0.8	2	0.1	0.5	0.6

corrosion protection efficiency. After 360 h of immersion, current density value of PDMS increased and polarization resistance decreased rapidly, indicating the deterioration of barrier activity. However, GSP coating even after 360 h of immersion showed three orders lower corrosion current density and four orders higher polarization resistance as compared to the uncoated specimen. The protective capability of the GSP coated specimen originates from the diffusion barriers protection by extended Si$-$O$-$Si cross linkage of PDMS and nano-SiO$_2$ and reduced galvanic coupling due to the PDMS overlay coating.

Figure 4(a) Effect of immersion time on open circuit potential (OCP) of the PDMS and GSP coated CS specimens in 3.5 wt.% NaCl solution at 1 h, 120 h, 240 h, and 360 h, (b) Tafel plots of uncoated and coated CS specimens in 3.5 wt.% NaCl solution.The PDMS coated surfaces showed severe corrosion and entire delamination of coating after post exposure to salt-spray test for 1000 h whereas, the GSP coated surface showed minimal corrosion deterioration and the scratched areas of GSP coated specimens were visible without any corrosion indication. The PDMS coating exhibit higher corrosion resistance at initial immersion period, however the corrosion resistance value decreased and then gradually increased. This variation in corrosion resistance property is due to percolation of the electrolyte through micro-pores of the coating. Once the electrolyte reaches the metal surface, corrosion takes place and the corrosion products formed will prevent further transport of corrosive ions. Even though, GSP coating showed similar trend in impedance behavior, the impedance value observed was higher than PDMS coating, indicating the better corrosion protection performance. GSP composite coating, in comparison to the GO and GS coatings, confirm the insulating property of PDMS overlay over GS on reducing the galvanic coupling.

Figure 5e–h depicts the CLSM image of total biofilm components such as protein, sugar, lipids, amino acid on uncoated and coated CS specimens. The fluorescence observed for protein content of biofilm on uncoated specimen was abundant, followed by GS coating, PDMS and GSP coated specimen. The other biofilm components such as lipid, amino acid and sugar are rarely seen in the biofilm observed on both uncoated and coated specimens due to the shorter time of exposure. The biofilm thickness estimated from orthogonal projection are 35 ± 3.3 μm, 23 ± 3.6 μm, 9 ± 1.5 μm, and 5 ± 0.8 μm for uncoated CS, GS, PDMS, and GSP coated specimens, respectively. These results indicate significant inhibition of biofilm on the PDMS and GSP specimens.

A polydimethylsiloxane based composite coating with an interlayer of graphene oxide-nano-SiO$_2$ coating on carbon steel is developed using anodic electrophoretic deposition. The chemisorption of PDMS on GS coating provided a strong interfacial interaction and adhesion. The observed impedance values of GSP and phase angle value confirm the excellent coating characteristics. The GSP coating showed a six order higher charge transfer resistance and polarization resistance values as compared to the uncoated CS. The galvanic coupling studies clearly showed that the incorporation of nano-SiO$_2$ with GO results increase the corrosion resistance. The higher cross linking of Si$-$O$-$Si network in the GSP coated specimen provided the long term protection. The excellent antibacterial activity and anti-biofouling properties of the new composite coating are attributed to the toxic effect of GO and poor bio-adhesion on PDMS surface due to enhanced surface stiffness due to Si$-$O$-$Si network. As the GSP coating on the CS surface showed a significant enhancement in corrosion protection performance in 3.5 wt.% NaCl solution and anti-biofouling property, it is promising for applications in marine environment.

News and Events

National Seminar on Welding Science and Technology (NSWEST 2021)
July 23 - 24, 2021

Inauguration function of NSWEST 2021 held on July 23, 2021 from Blue room, IGCAR

Shri G. Nageswara Rao, Chairman, Atomic Energy Regulatory Board (AERB) inaugurated the Two days seminar "National Seminar on Welding Science and Technology – Present Status & Future Direction (NSWEST 2021) remotely on July 23, 2021 from Mumbai. This seminar was organized by the Indian Institute of Welding (IIW) – Chennai branch on virtual platform from IGCAR, Kalpakkam and about 200 engineers, scientists, research scholars and industrial personal attended this seminar. In his inaugural address, Chairman, AERB emphasized the use of advance welding process like, electron beam welding and acceptance of automation in welding. He highlighted the importance of dissimilar weld joint in industries and effect of residual stresses on the performance of the weld joint. He touched upon post weld heat treatment (PWHT) of weld joints, ASME codal guidelines on thickness, stress corrosion cracking (SCC) in heat affected zone HAZ) of weldment, meeting leak before break (LBB) criteria for safety considerations and application of advanced non-destructive examination (NDE) techniques for quality assurance etc.

Inaugural address by Shri G. Nageswara Rao, Chairman, Atomic Energy Regulatory Board (AERB)

He further emphasized on in-situ repair welding, in-service inspection, integrity assessment and life extension of nuclear components. He suggested to accepted prefabrication as a criteria in nuclear industries to avoid site fabrication due to limitation at the site.

A total of 129 technical lectures covering welding skill development, weld inspection, weld automation, consumables development, coating, fabrication, residual stress, corrosion, repair welding, creep, fatigue and high temperature materials & their weldability related to nuclear power plants, thermal power plants, defense and space sector were presented in 23 sessions, including 2 Plenary Talks, 29 Keynote, 10 Invited talks and 80 contributory papers.

Reported by
Shri T. V. Prabhu, Head, CFED, MCMFCG
& Convener, NSWEST-2021

News and Events

Technology Transfer of "Portable High Volume Air Sampler"
August 25, 2021

Technology license and document on IGCAR's High Volume Air Sampler technology being handed over by Head, IC-IGCAR to Director of M/s First Source Impex Pvt. Ltd., Bengaluru

Portable high volume air sampler is a light-weight device, made of Fiber Reinforced Plastic (FRP) and has an inbuilt embedded controller to start, stop, log and to calculate the total volume of air sampled. This is employed to collect airborne particulates in a filter paper medium at desired flow rates up to 2800 lpm. The import-substitute technology has been developed at SQRMG, IGCAR as part of the 'Atma Nirbhar Bharat' mission of Government of India and devices have already been deployed for in-house air quality monitoring. The device finds applications in pollution control boards for collection of suspended particulate matter in monitoring environmental pollution and in industries discharging particulate effluents for the purpose of monitoring. This is used in nuclear installations for the collection of air samples to estimate air-borne radioactivity levels.

This technology was transferred to M/s First Source Impex Pvt. Ltd., Bengaluru on August 25, 2021 at a brief event coordinated by Incubation Centre-IGCAR. The meeting was attended by Dr. B. Venkatraman, Director SQRMG (IGCAR), Dr. N. Subramanian, Head, Incubation Centre-IGCAR, Dr. C. V. Srinivas, Head, EAD, SQRMG, Dr. V. Subramanian, Head, ATBS, RESD, SQRMG, Dr. S. Chandrasekaran, Head, EnAS, EAD, SQRMG, Dr. M. Menaka, Head, RAMS, RESD, SQRMG, Shri R. Rajesh Kumar (Director, First Source Impex Pvt Ltd., Bengaluru) and Shri B. Balakrishnan (First Source Impex Pvt Ltd., Bengaluru).

Reported by
Dr. N. Subramanian
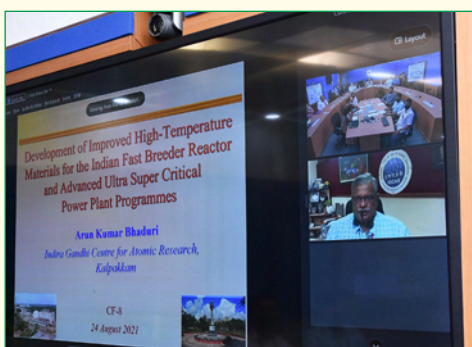*Head, Incubation Centre-IGCAR*

News and Events

Eighth International Conference on Creep, Fatigue and Creep-Fatigue Interaction (CF-8) [Web Conference]
August 24-27, 2021

Dr. R. Divakar, Associate Director, MEG, IGCAR, Dr. M. Vasudevan, Head, MDTD, IGCAR, Dr. B. Venkatraman, Director, IGCAR and Dr. Shaju K. Albert, Chairman, Local Organizing Committee, CF-8 and formerly, Director, MMG, IGCAR during the inaugural session of CF-8

The Eighth International Conference on Creep, Fatigue and Creep-Fatigue Interaction (CF-8), jointly organized by Indira Gandhi Centre for Atomic Research (IGCAR), Kalpakkam and the Metal Sciences Division and the Kalpakkam Chapter of the Indian Institute of Metals (IIM) was conducted as a Web Conference between 24.8.2021 and 27.8.2021. The conference was conducted in collaboration with the Japan Society of Mechanical Engineers (JSME) and was attended by about 150 scientists and engineers from India and abroad, specializing in the areas of creep, fatigue and their interaction. The inaugural address of the conference was delivered by the Chief Guest Sri. S. C. Chetal, Senior Scientific Advisor, Bharat Heavy Electricals Limited and former Director, IGCAR and Indian Mission on AUSC programme. He observed that high temperature design codes lay strong emphasis on the strength of materials whereas ductility does not directly enter into the analysis, adding that a proper balance between the two is essential to ensure structural integrity and safety of components subjected to high temperatures and high stresses during service. He also suggested that emphasis should be given in the areas of creep-fatigue interaction, unification of design factors among various codes, mechanical properties of weldments before and after repair welding, component testing, etc. from the viewpoint of long-term safety and integrity of components and structures. A total of 102 technical lectures covering creep, fatigue and their interaction aspects of various structural materials of interest to nuclear and fossil-fuel power plants, defence and aerospace sectors were presented in 23 sessions including 24 keynote and 6 plenary lectures by leading experts on the core theme of the conference. The concluding session of the conference identified several potential areas that could be included in the scope of the next conference of the CF-series. Prominent among them were testing under simulated environments, condition monitoring of ageing plants, testing requirements for strategic applications, miniaturization of specimen testing and thrust for physics-based modelling. Dr. Shaju K. Albert, Chairman, Local Organizing Committee, CF-8 presented a summary of the proceedings with a brief overview of the papers presented during the four days.

Plenary lecture being delivered by Dr. A.K. Bhaduri, the then director, IGCAR on August 24, 2021.

A total of 45 presentations delivered by Students and Young Scientists were included for consideration of best presentation awards. Three best presentations in each category were honoured with the awards comprising of citations and cash prizes.

Reported by
Dr. R. Divakar, Associate Director, MEG, IGCAR,

Awards and Honours

Dr. Sandip Kumar Dhara, Materials Science Group: Elected as a Fellow of the Institute of Physics, England.

Dr. Anish Kumar, Head, NDED has been selected as the Editorial Board member of journal Research in Nondestructive Evaluation (American Society for Nondestructive Testing).

Best Paper/Poster Awards

Best Paper Award

G. Sainath and A. Nagesha
"Atomistic simulations of twin boundary effect on the crack growth behaviour in BCC Fe".
8th International Conference on Creep, Fatigue and Creep-Fatigue Interaction (CF-8) held during August 24-27, 2021 at Indira Gandhi Centre for Atomic Research, Kalpakkam

Bio-diversity @ DAE Campus, Kalpakkam

Indian Silverbill

© SIRD, IGCAR

Indian Silverbill was formerly known as White-Throated Munias, a finch like bird with a pointed black and white tail. It has greyish-brown upperparts with a white rump and black wings. They are usually seen in small flocks and feeds on grass seeds and small insects.